




## Investigations on the shock wave induced by collapse of a toroidal bubble

Cheng Liu <sup>1,\*</sup>, Xiaobin Yang <sup>1</sup>, Jingqi Li,<sup>1</sup> Yiding Hu,<sup>1</sup> Min Zhao,<sup>1</sup> and Changhong Hu <sup>2</sup>

<sup>1</sup>*School of Naval Architecture, Ocean and Civil Engineering, Shanghai Jiao Tong University, Shanghai 200240, China*

<sup>2</sup>*Research Institute for Applied Mechanics, Kyushu University, Fukuoka 816-0811, Japan*



(Received 19 July 2023; accepted 28 June 2024; published 16 July 2024)

When bubbles collapse near a wall, they typically experience an asymmetric deformation. This collapse leads to the creation of a jet that strikes the bubble interface, causing the formation of a toroidal bubble and the subsequent release of a water-hammer shock. In this study, we present a systematic analysis of the collapse of a toroidal bubble in an open field or adjacent to a flat wall using high-fidelity numerical simulation. To maintain the sharpness of the interface, we employ the interface compression technique and the boundary variation diminishing approach within the two-phase model. Our findings demonstrate that shock waves emitted from the toroidal bubble consistently propagate toward the central axis of the torus, resulting in significant pressure shocks along the axis, similar to the water-hammer shock formed during the collapse of a spherical bubble. In contrast, weak pressure waves are generated in the transverse directions, leading to relatively weaker pressure peaks. Furthermore, the wall-pressure peak induced by the toroidal bubble is approximately three times higher than that induced by the spherical bubble. Based on the directional characteristics of pressure wave propagation from collapsing toroidal bubbles, toroidal-shaped pressure vessels can be designed as buoyancy materials for deep submersibles. This design enables the focused release of energy in a specific direction, effectively minimizing the destructive chain reaction caused by the implosion.

DOI: [10.1103/PhysRevE.110.015103](https://doi.org/10.1103/PhysRevE.110.015103)

### I. INTRODUCTION

The toroidal bubble is a common phenomenon in both natural and engineering applications, such as freely rising gas bubbles [1,2], shock-induced collapsing bubbles [3–5], bubble collapse near a free surface [6–10] or a solid wall [11–19], and multibubble interactions [20–23]. When a bubble collapses asymmetrically, the jet induced by the collapse can pierce the bubble and break it into a toroid. Numerous studies [8,24–27] have shown that the successive collapse and rebound of the toroidal bubble in the late stage can emit complex shock waves, which may cause damage to nearby structures. Moreover, Bempedelis and Ventikos [28] demonstrated that the existence of a toroidal bubble can strengthen the collapse of nearby bubbles, leading to a peak pressure up to 140 GPa in the flow field. Recently, researchers have also found that the toroidal bubble has different acoustic properties from the spherical bubble [29,30].

However, despite the widespread occurrence of toroidal bubbles, there are only a few studies concerning the collapse of a toroidal bubble. Chahine and Genoux [31] developed a theoretical toroidal bubble dynamical equation based on an asymptotic approach, but the cross section of the bubble ring was confined to a circle shape. Cao and Macián-Juan [32] simulated a spherical gas bubble rising in water, and found that the formation of a toroidal bubble after central breakup was heavily dependent on initial conditions. Liu *et al.* [15,33] used axisymmetric incompressible Navier-Stokes equations

and the front tracking method to study the toroidal bubble dynamics near a solid wall, and found that initial wall-bubble distance and liquid viscosity had significant effects on the evolution of the toroidal bubble. In summary, while some progress has been made in understanding the dynamics of toroidal bubbles, the formation mechanism of shock waves during the violent collapse of a toroidal bubble is still not fully understood. Further research is needed to address this gap in knowledge and to develop better models for predicting the behavior of toroidal bubbles in different applications.

Our research aims to improve the understanding of the shock wave characteristics and morphology features of toroidal bubble collapse using a high-fidelity numerical approach. To achieve this, we have adopted the interface compression technique to modify the compressible two-phase model of Kapila *et al.* [34]. This modification improves the sharpness of the phase interface and confines the interface span to a desired thickness. Additionally, we have used the boundary variation diminishing (BVD) principle [35,36] to construct the Weighted Essentially Non-oscillatory (WENO)-Tangent of Hyperbola for Interface Capturing (THINC)-BVD scheme for spatial reconstruction. This scheme, which employs the fifth-order WENO scheme [37] and the interface capturing function called THINC [38], minimizes numerical dissipation near any type of discontinuity, including contact discontinuities, shock waves, and phase interfaces. By a comprehensive analysis of the shock wave behavior in toroidal bubble collapse, we hope to provide insights into this complex phenomenon, thereby contributing to the optimization design of underwater pressure vessels.

\*Contact author: [chengliu@sjtu.edu.cn](mailto:chengliu@sjtu.edu.cn)

In the following work, we present our physical model, numerical implementation, and validation in Sec. II. We discuss the characteristics of shock waves and peak pressure induced by shock impacting in Sec. III. Finally, we summarize our important conclusions in Sec. IV.

## II. NUMERICAL METHODS

### A. Governing equations with interface sharpening terms

To improve the sharpness of a moving interface, the compressible two-phase five-equation model of Kapila *et al.* [34] with the interface compression technique [39] is employed. The governing equations are given by

$$\frac{\partial(\alpha_1\rho_1)}{\partial t} + \nabla \cdot (\alpha_1\rho_1\mathbf{u}) = -\rho_1\mathcal{R}(\alpha_2), \quad (1)$$

$$\frac{\partial(\alpha_2\rho_2)}{\partial t} + \nabla \cdot (\alpha_2\rho_2\mathbf{u}) = \rho_2\mathcal{R}(\alpha_2), \quad (2)$$

$$\frac{\partial(\rho\mathbf{u})}{\partial t} + \nabla \cdot (\rho\mathbf{u}\mathbf{u} + p) = (\rho_2 - \rho_1)\mathbf{u}\mathcal{R}(\alpha_2), \quad (3)$$

$$\begin{aligned} \frac{\partial(\rho E)}{\partial t} + \nabla \cdot [(\rho E + p)\mathbf{u}] \\ = [0.5(\rho_2 - \rho_1)|\mathbf{u}|^2 + p(\Gamma_2 - \Gamma_1) + \Pi_2 - \Pi_1]\mathcal{R}(\alpha_2), \end{aligned} \quad (4)$$

$$\frac{\partial\alpha_2}{\partial t} + \mathbf{u} \cdot \nabla\alpha_2 = \frac{\alpha_1\alpha_2(\rho_1c_1^2 - \rho_2c_2^2)}{\alpha_1\rho_2c_2^2 + \alpha_2\rho_1c_1^2} \nabla \cdot \mathbf{u} + \mathcal{R}(\alpha_2), \quad (5)$$

where  $\alpha_k$  is the volume fraction,  $\rho_k$  the density,  $\mathbf{u}$  the velocity vector,  $E$  the total energy, and  $p$  the pressure. The subscript  $k = 1$  refers to the liquid phase and  $k = 2$  the gas phase. The interface compression term  $\mathcal{R}(\alpha_2)$  on the right-hand side of the Eq. (5) is used to sharpen the phase interface,

$$\mathcal{R}(\alpha_2) = \mathcal{L}(\alpha_2)\chi_0\mathbf{n} \cdot \nabla[\epsilon|\nabla\alpha_2| - \alpha_2(1 - \alpha_2)], \quad (6)$$

where

$$\mathcal{L}(\alpha_2) = \begin{cases} 1, & 10^{-6} < \alpha_2 < 1 - 10^{-6} \\ 0, & \text{otherwise} \end{cases}. \quad (7)$$

The characteristic speed is

$$\chi_0 = 4[\alpha_2(1 - \alpha_2)|\mathbf{u}|]_{\max}. \quad (8)$$

The interface normal is

$$\mathbf{n} = \nabla\alpha_2/|\nabla\alpha_2|. \quad (9)$$

The parameter  $\epsilon$  is used to define the desired interface thickness; we set  $\epsilon = 0.75\Delta x_{\min}$  following the work of Tiwari *et al.* [39], where  $\Delta x_{\min}$  is the finest mesh size. The thickness of the interface is maintained by a balance between the sharpening term  $\alpha_2(1 - \alpha_2)$  and diffusion term  $\epsilon|\nabla\alpha_2|$ . The  $\mathcal{R}$ -like terms in Eqs. (1)–(4) are designed to satisfy the need for thermodynamical consistency within the interface region. The stiffened gas equation of state (SG EOS) [40] is used to close the governing equations,

$$p = (\pi - 1)\rho e - \pi p_\infty, \quad (10)$$

where  $\pi$  is the ratio of specific heats,  $p_\infty$  the stiffness constant, and  $e$  the density of internal energy. The states of

mixture flow is given by

$$\alpha_1 + \alpha_2 = 1, \quad (11)$$

$$\alpha_1\rho_1 + \alpha_2\rho_2 = \rho, \quad (12)$$

$$\frac{\alpha_1}{\pi_1 - 1} + \frac{\alpha_2}{\pi_2 - 1} = \frac{1}{\pi - 1}, \quad (13)$$

$$\frac{\alpha_1 p_{\infty,1}}{\pi_1 - 1} + \frac{\alpha_2 p_{\infty,2}}{\pi_2 - 1} = \frac{p_\infty}{\pi - 1}. \quad (14)$$

In this paper, we adopt dimensionless parameters according to previous works in the literature [3,41,42]. For the gas phase  $\pi_2 = 1.4$  and  $p_{\infty,2} = 0$ ; for the liquid phase  $\pi_1 = 6.59$ , and  $p_{\infty,1} = 4049$ . The sound speed is computed by the mixture variables as

$$c^2 = \frac{\pi(p + p_\infty)}{\rho}, \quad (15)$$

and the time step is calculated by

$$\Delta t = \frac{\Delta x_{\min}}{||\mathbf{u}| + c|_{\max}}. \quad (16)$$

In this study, the boundary conditions are specified at the ghost cell of the boundary face. The zero-order extrapolation boundary conditions as follows are considered for the far field of computational domain,

$$d\mathbf{q}/dx|_\Gamma = \mathbf{0}, \quad (17)$$

where  $\Gamma$  indicates the boundary face and  $\mathbf{q} = [\alpha_1, \alpha_2, \rho_1, \rho_2, u, v, w, p]^T$ . The boundary conditions for the wall are the same as the zero-order extrapolation conditions except for the velocity  $\mathbf{u} = (u_n, u_\zeta, u_\eta)$ , in which the normal component to the wall boundary,  $u_n$ , must be prescribed at ghost cells to ensure

$$u_n|_\Gamma = 0. \quad (18)$$

The boundary condition for other velocity components,  $u_\zeta$  and  $u_\eta$ , follows Eq. (17).

### B. Numerical discretization

The BVD scheme replaces the reconstruction of high-order schemes like Monotone Upstream-centered Schemes for Conservation Laws [43] or WENO [37] with an interface capturing function called THINC [38] to minimize variations (jumps) of reconstructed variables at cell boundaries, thereby effectively reducing numerical dissipation. In this paper, we consider the fifth-order WENO scheme and the THINC function as two candidates for the spatial reconstruction, and the so-called WENO-THINC-BVD scheme is constructed [35]. To enhance the accuracy and avoid spurious oscillations, we reconstruct the primitive variables at cell boundaries [3,44,45]. The numerical fluxes are evaluated using the wave propagation method [46] and the HLLC (Harten–Lax–van Leer contact) Riemann solver [47], which is known for its high accuracy and ability to capture shocks. Additionally, the source terms in the governing equations are calculated using a centered scheme. Finally, we update the time using the third-order Runge-Kutta scheme [48]. The detailed implementation of the present numerical algorithm can be found in our previous work [49].

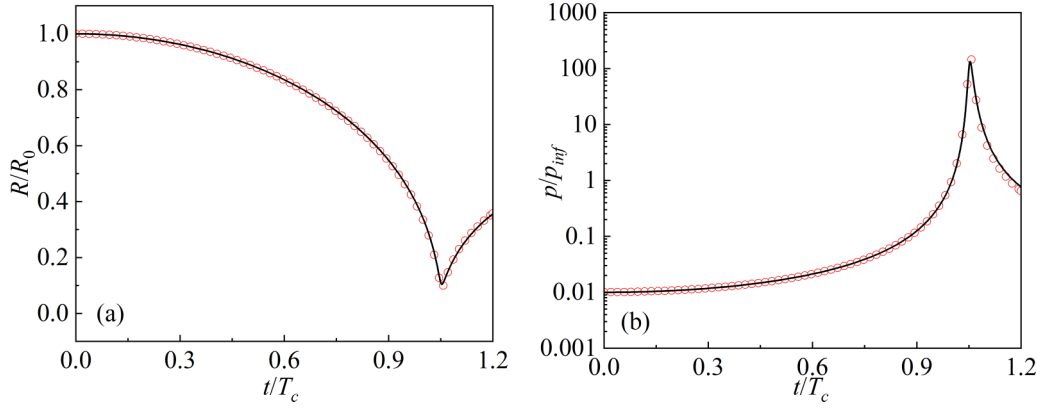


FIG. 1. Collapse of a single bubble in an open space with initial driven pressure  $p_{inf}/p_0 = 100$ , and initial radius  $R_0 = 3.64 \times 10^{-4}$  m. (a) Average bubble radius; (b) average bubble pressure. (—) solutions from the KM equation [50]; (○) present results.

### C. Validations

To evaluate the effectiveness and dependability of our algorithm, we simulate the collapse of a single bubble in a free field with a driven pressure of  $p_{inf}/p_0 = 100$ , where  $p_{inf}$  represents the initial ambient pressure and  $p_0$  represents the initial pressure of the bubble. We utilize a cubic computational domain with dimensions of  $x, y, z \in [0, 20R_0]$ , where

$R_0$  is the initial radius of the bubble. The average bubble radius is computed by the average bubble volume using the formula

$$V = \sum_{\Omega} (\Delta x \Delta y \Delta z)_i \alpha_i, \quad (19)$$

and the average bubble pressure is calculated by

$$p = \frac{1}{V} \sum_{\Omega} (\Delta x \Delta y \Delta z)_i \alpha_i p_i. \quad (20)$$

In these formulas,  $\alpha_i$ ,  $(\Delta x \Delta y \Delta z)_i$ , and  $p_i$  refer to the gas volume fraction, volume, and pressure of the  $i$ th cell, respectively, and  $\Omega$  denotes the computational domain. Our results, as shown in Fig. 1, demonstrate that the time histories of the average bubble radius and pressure closely match the theoretical solutions from the Keller-Miksis (KM) equation [50]. To normalize time, we use the Rayleigh collapse time formula for the spherical bubble [51]:

$$T_c = 0.915 R_0 \sqrt{\frac{\rho_{inf}}{(p_{inf} - p_0)}}, \quad (21)$$

where  $\rho_{inf}$  is the initial ambient density.

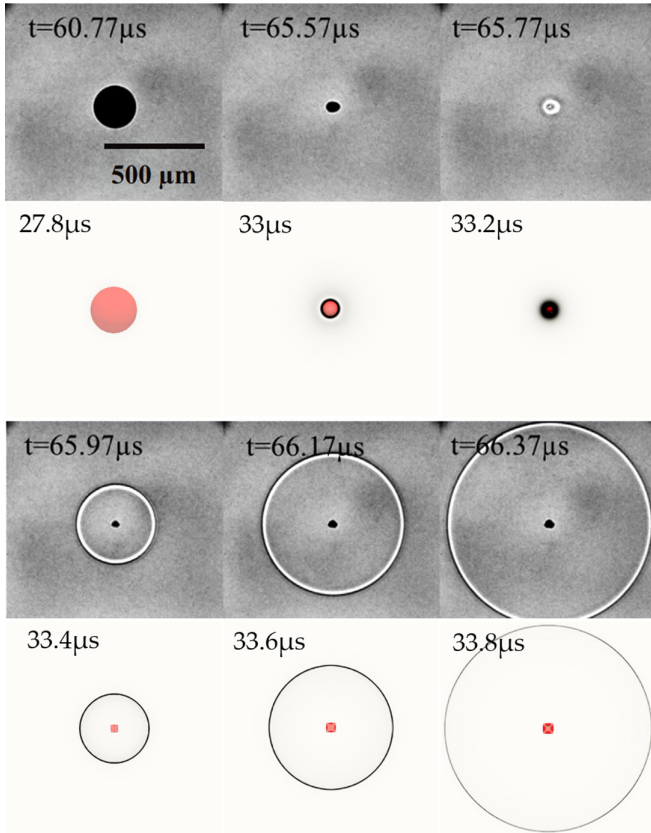


FIG. 2. Comparison of present numerical results ( $|\nabla p|$ ) with the laser-induced bubble experiments [52] for the collapse of a single bubble in an open space, where the initial driven pressure is  $p_{inf}/p_0 = 2083$ , and initial radius  $R_0 = 3.64 \times 10^{-4}$  m; the red surface is the isosurface of  $\alpha_2 = 0.5$ .

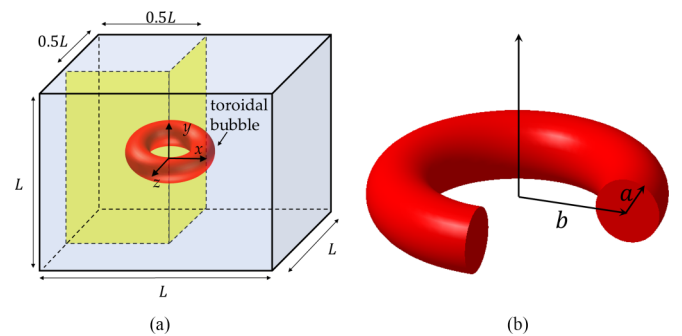


FIG. 3. Numerical setup for the collapse of a toroidal bubble. (a) Computational domain; the red torus denotes the toroidal bubble, and the symmetry boundary conditions are applied on the yellow cross sections. (b)  $b$  is the major radius of the toroidal bubble (distance between the center of the toroidal bubble and the center of its circular cross section) and  $a$  the minor radius.

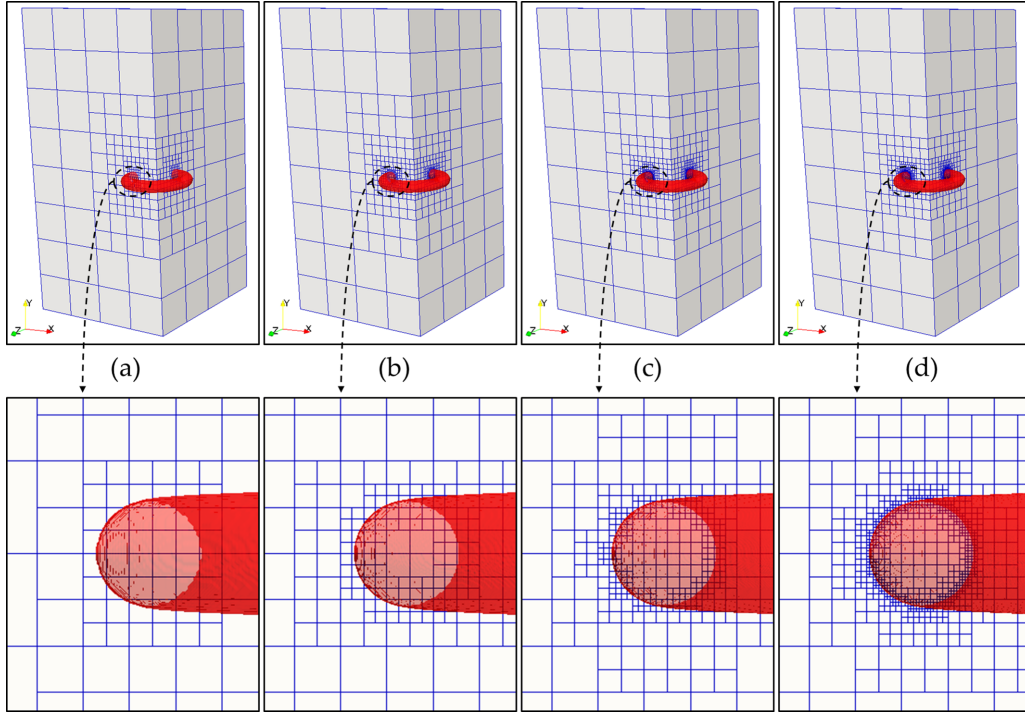


FIG. 4. Initialized mesh blocks of the refinement levels (a) 3–7, (b) 3–8, (c) 3–9, and (d) 3–10 for the collapse of a toroidal bubble in an open space with  $\varepsilon = 5$  and  $p_{\text{inf}}/p_0 = 100$ . The lower row gives the enlargement region near the bubble surface. Each mesh block is evenly divided by  $8 \times 8 \times 8$  cells. The red surface denotes the isosurface of  $\alpha_2 = 0.5$ .

We also simulate a bubble collapse in an open space and compare our results with the laser-induced bubble experiment carried out by Johansen *et al.* [52]. The experimental conditions indicate that the maximum radius of the bubble is approximately  $R_{\text{max}} = 3.64 \times 10^{-4}$  m, and the initial bubble driven pressure  $p_{\text{inf}}/p_0 = 2083$ . The collapse process is depicted in Fig. 2, where it is revealed that the bubble collapses spherically at the initial stage. As the bubble reaches its minimum volume, it undergoes a rebound, emitting a radially propagating shock wave. Notably, both the bubble shape and shock front closely align with experimental results; this validation further underscores the capability of our algorithm in providing precise simulations of bubble collapse dynamics and shock wave propagations.

### III. RESULTS AND DISCUSSION

#### A. Collapse in an open space

The violent implosion of underwater pressure vessels due to a sudden loss of structural stability can give rise to a high-intensity shock wave, which may cause significant damage to nearby structures; therefore the geometric structure of underwater pressure vessels should be considered to minimize the influence of implosion. In this section, we consider the collapse of a toroidal bubble in an open field as shown in Fig. 3. The toroidal bubble is initially placed at the center of the computational domain. For comparison, we keep the initial volume of the toroidal bubble  $V_0 = 1 \text{ m}^3$ , which is equivalent

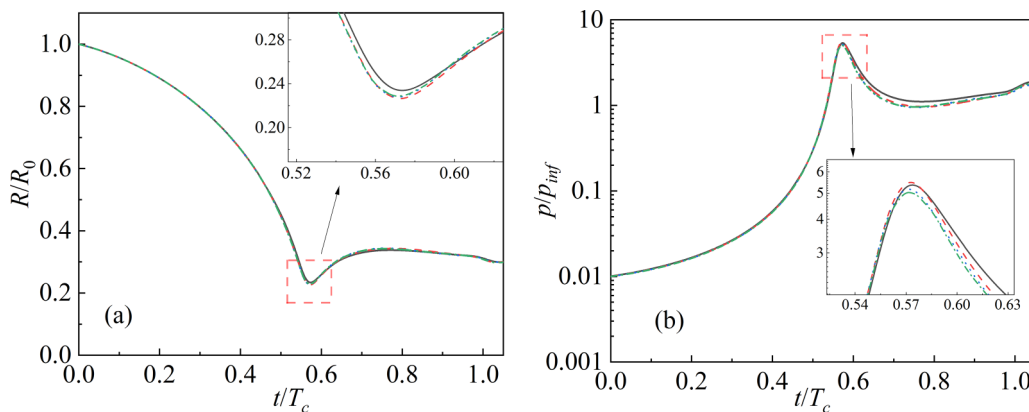


FIG. 5. Grid convergence study of the collapse of a toroidal bubble in an open space with  $\varepsilon = 5$  and  $p_{\text{inf}}/p_0 = 100$ . Time histories of (a) average bubble radius and (b) average bubble pressure. Mesh refinement level (—) 3–7; (---) 3–8; (···) 3–9; (-·-·) 3–10.

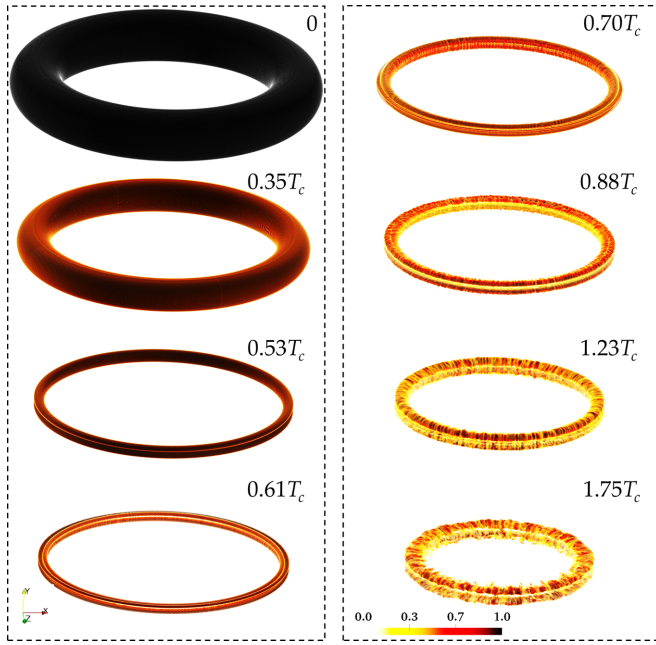


FIG. 6. Collapse of toroidal bubble with  $\varepsilon = 5$  and  $p_{\text{int}}/p_0 = 100$  (rendered by volume fraction  $\alpha_2$ ).

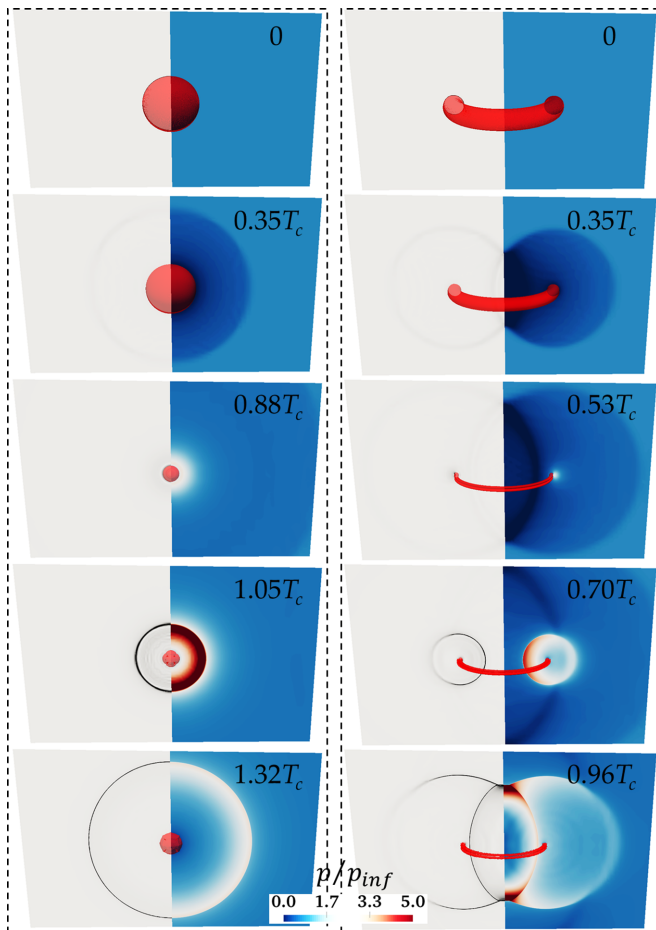


FIG. 7. Pressure gradient  $|\nabla p|$  (left) and pressure (right) of the collapse of a single and a toroidal bubble ( $\varepsilon = 5$ ) in an open field. The driven pressure is  $p_{\text{int}}/p_0 = 100$ . The red surface is the isosurface of  $\alpha = 0.5$ .

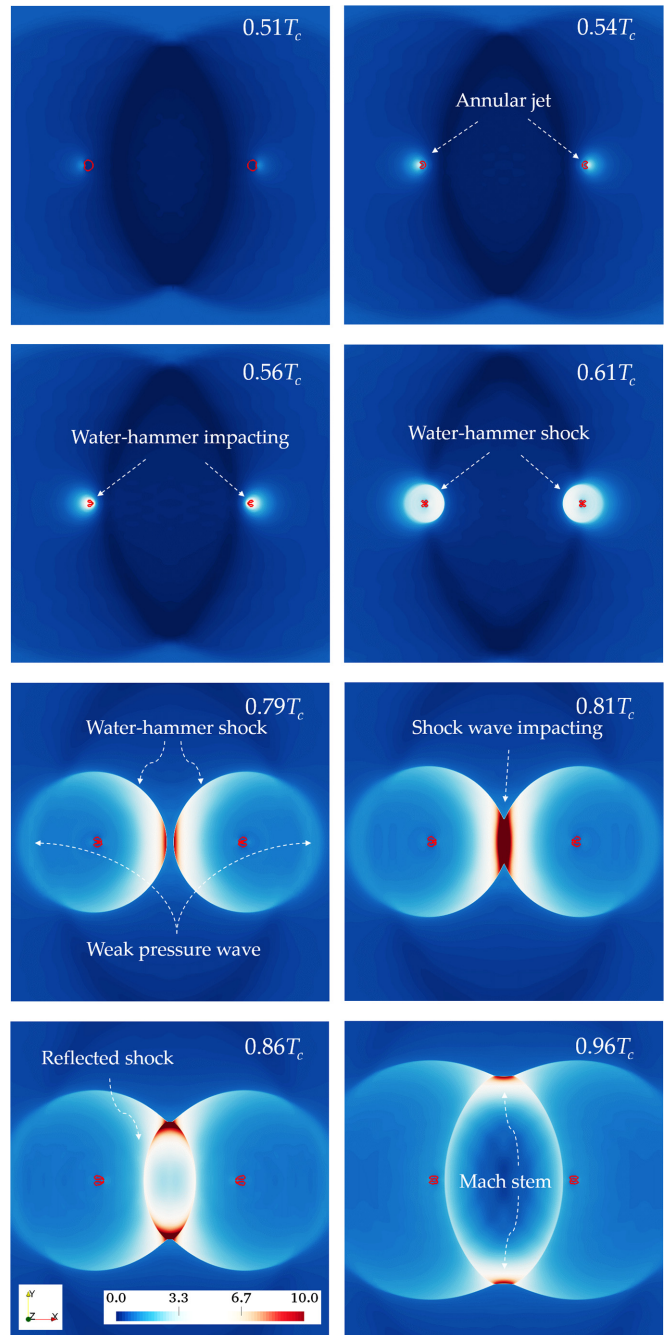


FIG. 8. Pressure contour on the cross section  $z = 0$  during the collapse of a toroidal bubble with  $\varepsilon = 5$  and  $p_{\text{int}}/p_0 = 100$ . The red line is the isosurface of  $\alpha = 0.5$ .

to a spherical bubble with initial bubble radius  $R_0 \approx 0.62$  m. The volume of the toroidal bubble is calculated by

$$V = (2\pi b)\pi a^2,$$

and the aspect ratio is defined by

$$\varepsilon = b/a.$$

Considering the average speed of a bubble (with  $R_0$ ) collapsing in water,  $\sqrt{p_l/\rho_l}$ , and waterlike kinematic viscosity,  $\nu = 10^{-6} \text{ m}^2 \text{ s}^{-1}$ , the Reynolds number is  $3.92 \times 10^8$ ; thus neglecting viscosity in the simulation is reasonable.

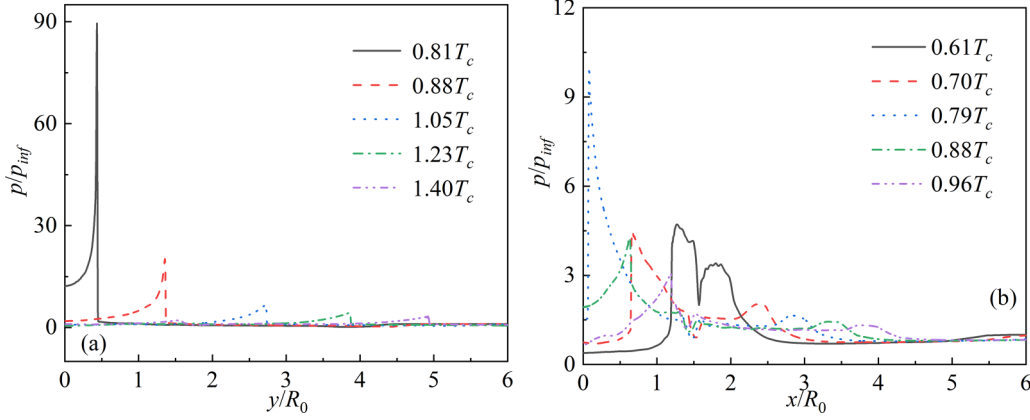


FIG. 9. Pressure distributions on the  $y$  axis (a) and  $x$  axis (b) during the collapse of a toroidal bubble with  $\varepsilon = 5$  and  $p_{\text{inf}}/p_0 = 100$ . Here,  $x = 0$  refers to the location of the torus center and  $x = 1.74R_0$  refers to the center of the torus tube.

Similarly, the Weber number for the present bubble collapsing simulation is  $2.87 \times 10^5$  when the air-water surface tension is  $0.072 \text{ N m}^{-1}$ , which also indicates the surface tension can be neglected.

The computational domain has dimensions  $x$ ,  $y$ , and  $z$  ranging from 0 to  $20L$ , where  $L$  is equal to  $20R_0$ . The inertial collapse process is initiated by the driven pressure,  $p_{\text{inf}}/p_0$ . To optimize computational resources, we implement symmetry boundary conditions on the yellow sections, effectively reducing the resolved domain to one-quarter of its original size.

In the simulation, we adopt parameters referring to previous works in the literature [3,41,42] and the detailed initial states are summarized in Table I.

The convergence study is conducted first. We simulate the collapse of the toroidal bubble in an open space with refinement levels of 3–7, 3–8, 3–9, and 3–10, where the finest refinement levels 7, 8, 9, and 10 correspond to  $R_0/\Delta x_{\text{min}} = 25.6, 51.2, 102.4, \text{ and } 204.8$ . The initial mesh blocks are presented in Fig. 4; each mesh block is evenly discretized by  $8 \times 8 \times 8$  cells. It can be found that as the refinement level increases, the region near the bubble surface is covered by the finer mesh blocks. The time histories of average bubble radius and bubble pressure are given in Fig. 5. The overall evolutions of bubble radius and bubble pressure show good agreement. However, slight discrepancies near the peak values (the enlarged regions in the red square) are observed, and the numerical results of refinement levels 3–8, 3–9, and 3–10 agree well with each other. To save computing resources, the refinement level 3–9 is applied in the following work.

Figure 6 illustrates the evolution of the toroidal bubble shape throughout the process. During the collapse stage, the bubble undergoes noticeable shrinkage in both the major and minor radius dimensions. At  $0.53T_c$ , the outer rim of the

bubble experiences an inward dent, leading to the formation of two separate torus bubbles at  $0.61T_c$ . As time progresses, the inner circle of the torus rapidly rebounds at  $0.70T_c$ . After the time instant  $0.88T_c$ , the bubble surface starts to exhibit ruffling, and a significant and intricate deformation of the bubble surface becomes apparent between the time intervals of  $1.23T_c - 1.75T_c$ . Throughout the collapse process, it is worth noting that the overall volume of the bubble ring consistently moves toward the center of the torus.

Figure 7 presents a comparison of the shock wave emission processes during the collapse of a spherical bubble and a toroidal bubble. Notably, the shock patterns observed in these two cases exhibit significant differences. In the case of a spherical bubble collapse, the collapse occurs spherically, and as the bubble reaches its minimum volume, a uniformly distributed high-pressure region forms around the bubble. Consequently, upon rebounding, the emitted shock wave propagates outward radially from the bubble center. In contrast, during the collapse of a toroidal bubble, a distinct high-pressure region emerges on the outer rim of the bubble. This localized high-pressure area leads to an inward denting of the bubble surface, generating a shock wave that propagates toward the centerline of the torus. This behavior is reminiscent of the collapse of a single bubble near a solid wall. At  $0.96T_c$ , the incident shock wave impacts the central axis of the ring in the toroidal bubble case. Following this impact, two reflected shocks are observed propagating in opposite directions, resulting in additional complex dynamics in the shock wave propagation process.

Figure 8 displays the pressure contour on the cross section  $z = 0$ , showcasing the dynamics of the shock wave propagation. During  $0.51-0.54T_c$ , the outer rim of the bubble begins to involute and a liquid jet is observed. Shortly after, the jet impacts on the inner rim of the bubble at  $0.56T_c$  giving rise to the generation of “water-hammer” shock at  $0.61T_c$ , which resembles the collapse of a spherical bubble near the solid wall [18]. As the shock wave travels, a region of high pressure forms behind its tip at  $0.79T_c$ . Subsequently, when the two shock waves collide with each other, a high-pressure zone emerges in the flow field at  $0.81T_c$ . It is worth noting that following the collision, a persistent high-pressure region appears at the interaction site, where the incident shock and

TABLE I. Initial conditions for the toroidal bubble with  $p_{\text{inf}}/p_0 = 100$ .

	$\rho$ (kg/m <sup>3</sup> )	$u$ (m/s)	$p$ (bars)	$\pi$	$p_\infty$ (bars)
Liquid	1000	0	1000	6.59	4049
Bubble	1	0	10	1.4	0

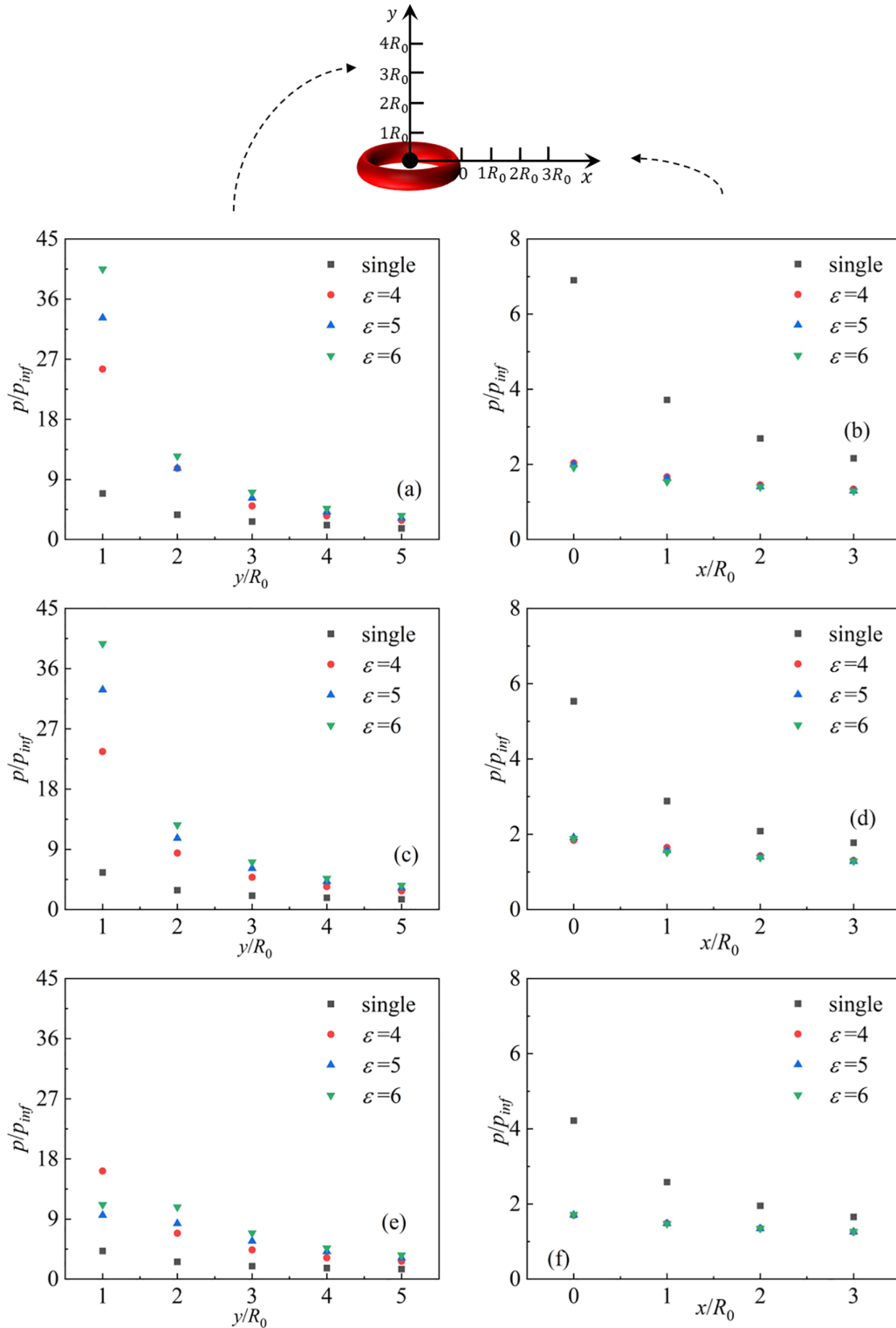


FIG. 10. Pressure peaks on the  $y$  axis and  $x$  axis during the collapse of a toroidal bubble with (a), (b)  $p_{inf}/p_0 = 100$ , (c), (d)  $p_{inf}/p_0 = 50$ , and (e), (f)  $p_{inf}/p_0 = 25$ . For comparison, we reset  $x = 0$  at the outer rim of the toroidal bubble.

the reflected shock meet ( $0.86\text{--}0.96T_c$ ). In the later stages, the interaction between the shock waves ultimately gives rise to the formation of a Mach stem, accompanied by the generation of high pressure at  $0.96T_c$ . This Mach stem represents a region where the shock waves interact and intensify, leading to the development of significantly elevated pressures.

To gain a deeper understanding of the dynamic behavior of toroidal bubbles, we conducted an analysis of the shock pressures exerted along both the axial and transverse directions. In Fig. 9(a), we observe that the peak pressure decreases rapidly as the distance from the center of the torus increases. Initially, the pressure peak can reach approximately  $\sim 90p_{inf}$  at a lo-

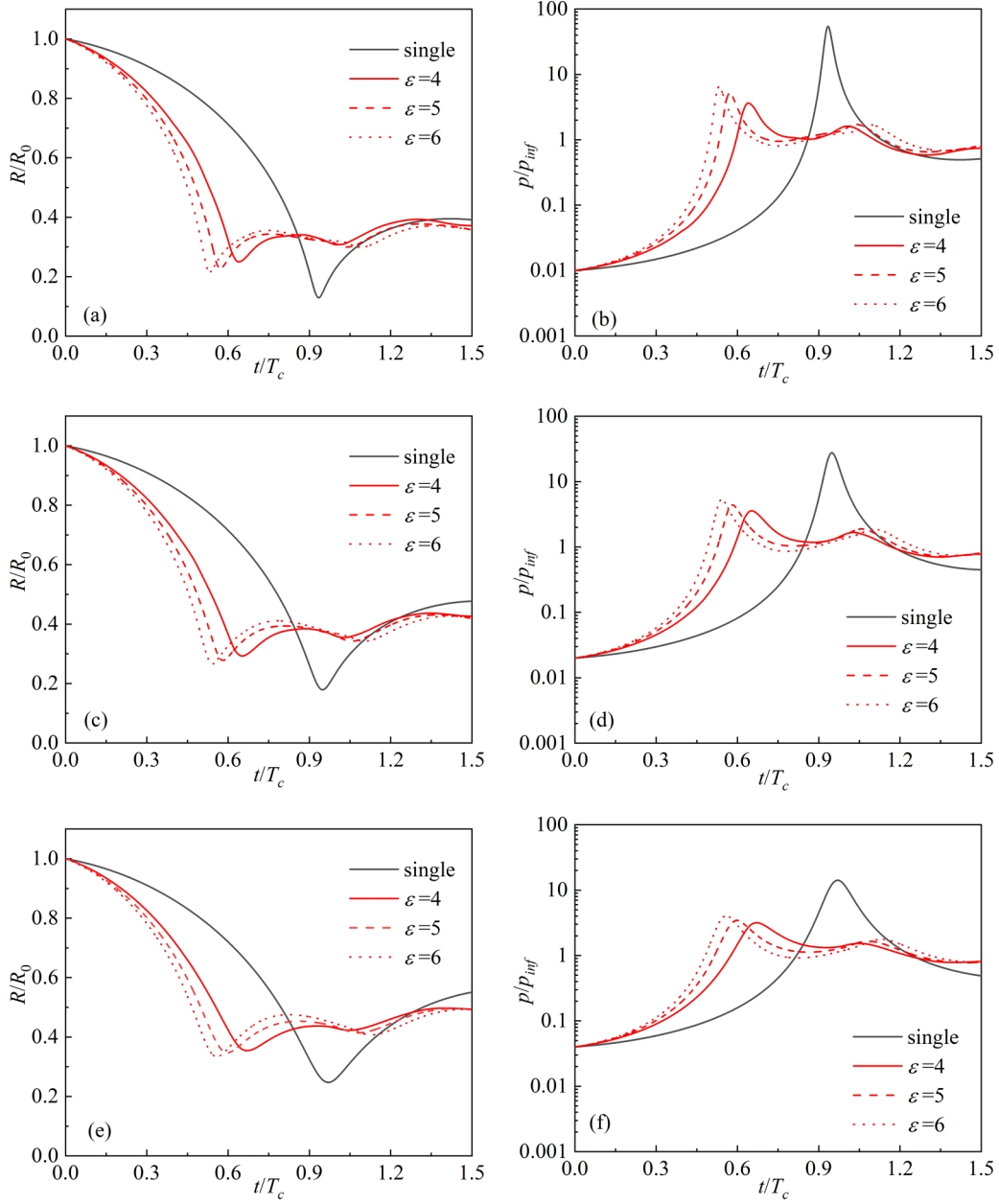


FIG. 11. Time evolutions of average bubble radius and average bubble pressure. The driven pressure is (a), (b)  $p_{\text{inf}}/p_0 = 100$ , (c), (d)  $p_{\text{inf}}/p_0 = 50$ , and (e), (f)  $p_{\text{inf}}/p_0 = 25$ .

cation near  $y \approx 0.5R_0$ . However, as it moves further away from the torus center, the peak pressure decreases rapidly to  $\sim 27p_{\text{inf}}$  at  $y \approx 1.4R_0$ , and to  $\sim 6.2p_{\text{inf}}$  at  $y \approx 2.7R_0$ . In Fig. 9(b), we also note that the maximum peak pressure induced by the weak pressure wave from the bubble center is comparatively lower. At  $x \approx 1.8R_0$ , the peak pressure due to the weak pressure wave is only  $\sim 3.4p_{\text{inf}}$ , while at  $x \approx 2.4R_0$ , it reaches approximately  $\sim 2.0p_{\text{inf}}$ . Despite the rapid dissipation of the pressure peak in both the axial and transverse directions, it is evident that the shock pressure in the axial direction remains significantly higher than that in the transverse direction. This highlights the importance of considering the asymmetry and directional dependencies in the shock pressure distribution of toroidal bubbles.

Figure 10 provides a comprehensive summary of the peak pressures for different aspect ratios  $\varepsilon$  and driven pressures  $p_{\text{inf}}/p_0$ , in the toroidal bubble cases. The results demonstrate that both the aspect ratio and driven pressure significantly influence the pressure near the center of the toroidal bubble. For the cases with driven pressure,  $p_{\text{inf}}/p_0 = 100$  and  $p_{\text{inf}}/p_0 = 50$ , the pressure peaks at  $y = 1.0R_0$  have large values ( $>40p_{\text{inf}}$ ). However, in the case of  $p_{\text{inf}}/p_0 = 25$ , the pressure peak at  $y = 1.0R_0$  decreases to be smaller than  $20p_{\text{inf}}$ . Interestingly, when  $y \geq 2.0R_0$ , the pressure peak is not notably affected by the aspect ratio or driven pressure. The peak pressures at these distances demonstrate similar magnitudes, particularly for  $y \geq 3.0R_0$ . In the transverse direction, the pressure peaks induced by the weak pressure wave are relatively small and show minimal sensitivity to



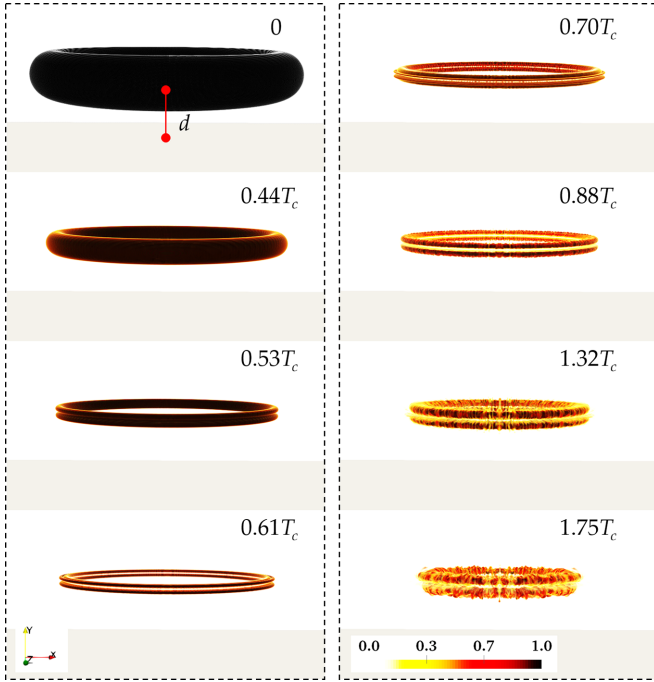


FIG. 12. Collapse of a toroidal bubble near a solid wall with  $\gamma = 2.5$ ;  $d$  refers to the distance between the torus center and a solid wall (rendered by volume fraction  $\alpha_2$ ).

the driven pressure or aspect ratio. Figure 10 reveals that the peak pressures in the axial direction consistently surpass those generated by the collapse of a spherical bubble. Conversely, the peak pressures in the transverse direction are significantly lower compared to the spherical case. This finding is crucial as it suggests that the toroidal bubble shape significantly alters the propagation process of shock waves, confining the high-pressure impact load primarily in the axial direction of the toroidal bubble.

Figure 11 showcases the temporal evolution of the average bubble radius and bubble pressure, revealing distinct differences between toroidal and spherical bubbles. Firstly, we observe that the toroidal bubble exhibits a faster collapse compared to the spherical bubble. The collapse time of the toroidal bubble remains approximately constant at around  $0.6T_c$  for all test cases, while the spherical bubble reaches its minimum collapse radius at approximately  $0.94T_c$ . Furthermore, there is a noticeable disparity in the strength of the collapse between the two bubble shapes. The minimum collapse radius of the spherical bubble is  $\sim 0.13R_0$  and the maximum collapse pressure reaches  $\sim 54p_{\text{inf}}$  for a driven pressure of  $p_{\text{inf}}/p_0 = 100$ . On the other hand, the minimum collapse radii of the toroidal bubble decrease as the aspect ratio  $\varepsilon$  increases. For  $\varepsilon$  values ranging from 4 to 6, the minimum collapse radii range from approximately  $0.25R_0$  to  $0.22R_0$ . At the same time, the corresponding maximum collapse pressures increase, ranging from approximately  $\sim 3.63p_{\text{inf}}$  for  $\varepsilon = 4$  to  $\sim 6.30p_{\text{inf}}$  for  $\varepsilon = 6$ . This implies that larger values of  $\varepsilon$  lead to more pronounced and violent behavior in the toroidal bubble. For the driven pressures of  $p_{\text{inf}}/p_0 = 50$  and  $p_{\text{inf}}/p_0 = 25$ , the collapse radius of the spherical bubble remains smaller than that of the toroidal bubble, and the collapse pressure of the spherical

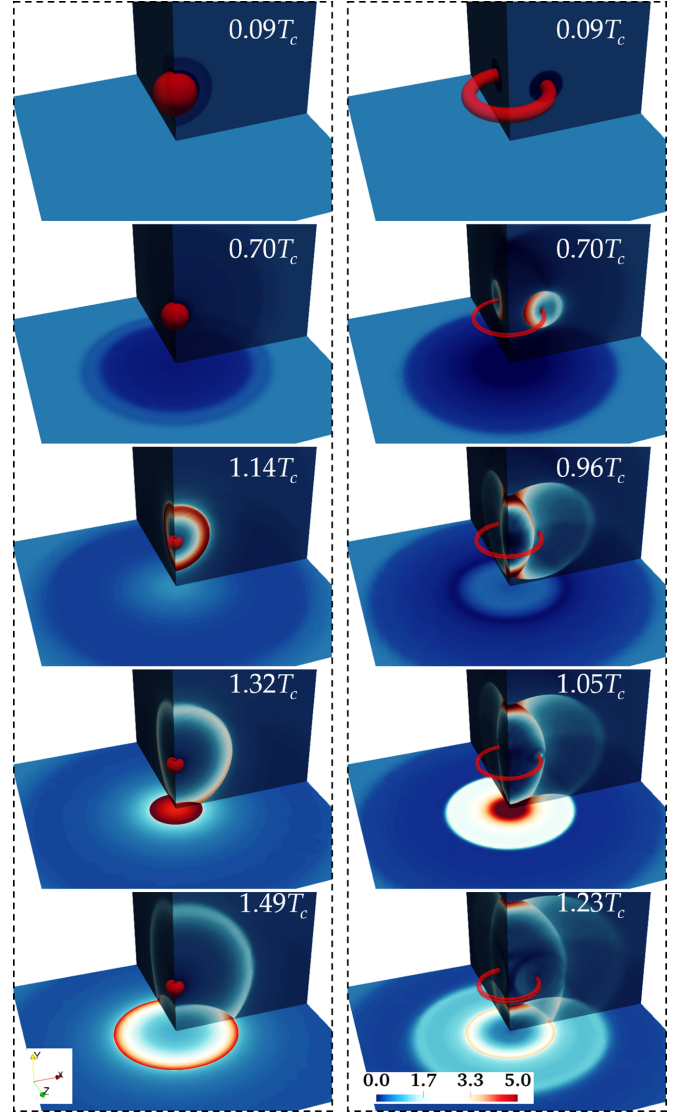


FIG. 13. Pressure distributions on the solid wall and cross sections  $x = 0$  and  $y = 0$  during the collapse of spherical bubble (left row) and a toroidal bubble (right row) near a solid wall with  $\gamma = 2.5$ .

bubble exceeds that of the toroidal bubble. However, although the collapse of the toroidal bubble is not as violent as the spherical bubble, it generates significantly higher pressures in the axial direction.

### B. Collapse near a solid wall

In this section, we present a comparison of pressure loads resulting from the collapses of toroidal and spherical bubbles in close proximity to a solid wall. The toroidal bubbles considered in this study have a fixed aspect ratio ( $\varepsilon = 5$ ) and are subjected to a driven pressure of  $p_{\text{inf}}/p_0 = 100$ . Figure 12 illustrates the evolution of the toroidal bubble shape near the solid wall. To quantify the wall-bubble distance, we introduce the nondimensional parameter  $\gamma$ , defined as  $\gamma = d/R_0$ , where  $d$  represents the distance between the center of the torus and the solid wall, and  $R_0$  denotes the initial radius of the toroidal bubble. Upon closer examination of the figure, it becomes

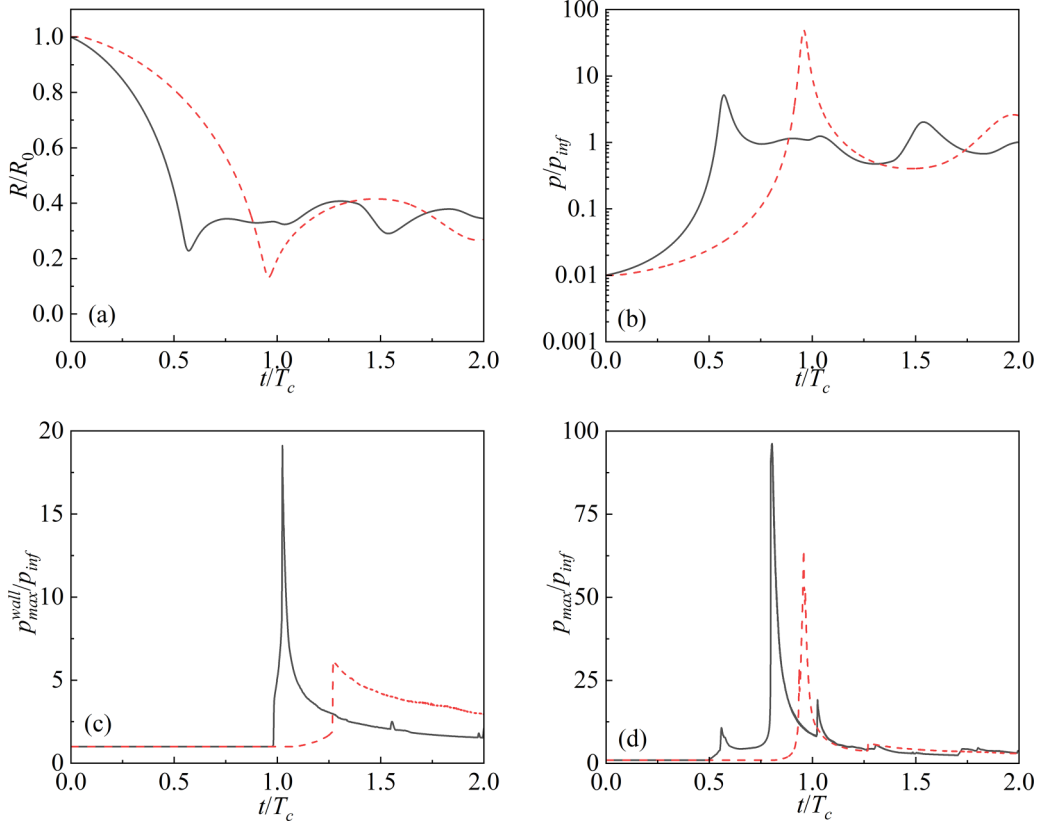


FIG. 14. Collapse of a toroidal bubble and a spherical bubble near a solid wall with  $\gamma = 2.5$ . Time histories of (a) average bubble radius, (b) average bubble pressure, (c) maximum wall pressure, and (d) maximum pressure in the computational domain. (—) Toroidal bubble; (---) spherical bubble.

evident that the toroidal bubble undergoes a series of distinct stages near the solid wall. Initially, the bubble experiences a shrinking phase, followed by a rebounding phase; in the later stages, the bubble undergoes violent deformation. The overall collapse process is similar to the toroidal bubble oscillating in the open space. The only deviation is the asymmetric deformation observed at  $1.75T_c$ .

Figure 13 illustrates the pressure wave emission processes of both the spherical and toroidal bubbles. Upon closer examination, it is evident that the spherical bubble's overall shape moves closer to the solid wall as it collapses, while the emitted shock wave propagates outward in a radial fashion. The impact of the downward shock front on the solid wall leads to the generation of high wall pressure, a phenomenon that has been extensively discussed in our previous work [18]. On the other hand, the shock wave emitted by the toroidal bubble moves toward the center axis, resulting in the formation of a peak pressure at the intersection of the incident and reflected shocks. As the shock waves focus on the solid wall, a region of high wall pressure becomes apparent at  $1.05T_c$ . Shortly thereafter, the shock waves interact with the solid wall in a circular pattern, and the shock pressure gradually dissipates over time.

Figure 14 presents the time histories of various parameters, including the average bubble radius, average bubble pressure, maximum wall pressure, and maximum pressure in the flow field. Upon analysis of Figs. 14(a) and 14(b), it becomes apparent that the toroidal bubble undergoes a faster collapse

compared to the spherical bubble. Additionally, the minimum bubble radius of the toroidal bubble is larger than that of the spherical bubble, while the corresponding maximum bubble pressure of the toroidal bubble is smaller. These observations suggest that the collapse of the spherical bubble is more violent compared to the toroidal bubble. However, examining Figs. 14(c) and 14(d) reveals an interesting contrast. The peak wall pressure and peak pressure in the flow field induced by the toroidal bubble are significantly larger, with values of  $19p_{\text{inf}}$  and  $96p_{\text{inf}}$ , respectively, whereas those induced by the spherical bubble are comparatively smaller, measuring  $6.1p_{\text{inf}}$  and  $64p_{\text{inf}}$ .

Figure 15 provides further insights into the collapse of toroidal and spherical bubbles at various wall-bubble distances, ranging from  $\gamma = 1.5$  to  $3.0$ . Upon examination of Figs. 15(a) and 15(b), it is evident that the toroidal bubble reaches a minimum bubble radius of approximately  $0.23R_0$ , accompanied by a maximum average bubble pressure of approximately  $5p_{\text{inf}}$ . In contrast, the spherical bubble exhibits a decrease in the minimum bubble radius from  $0.19R_0$  at  $\gamma = 1.5$  to  $0.13R_0$  at  $\gamma = 3.0$ , which is smaller than that of the toroidal bubble. However, the corresponding maximum bubble pressure for the spherical bubble increases significantly from  $14p_{\text{inf}}$  to  $57p_{\text{inf}}$ , surpassing that of the toroidal bubble. Moving on to Fig. 15(c), it is interesting to note that the peak wall pressure decreases as the wall-bubble distance  $\gamma$  increases. Notably, the peak wall pressure induced by the toroidal bubble is approximately three times higher

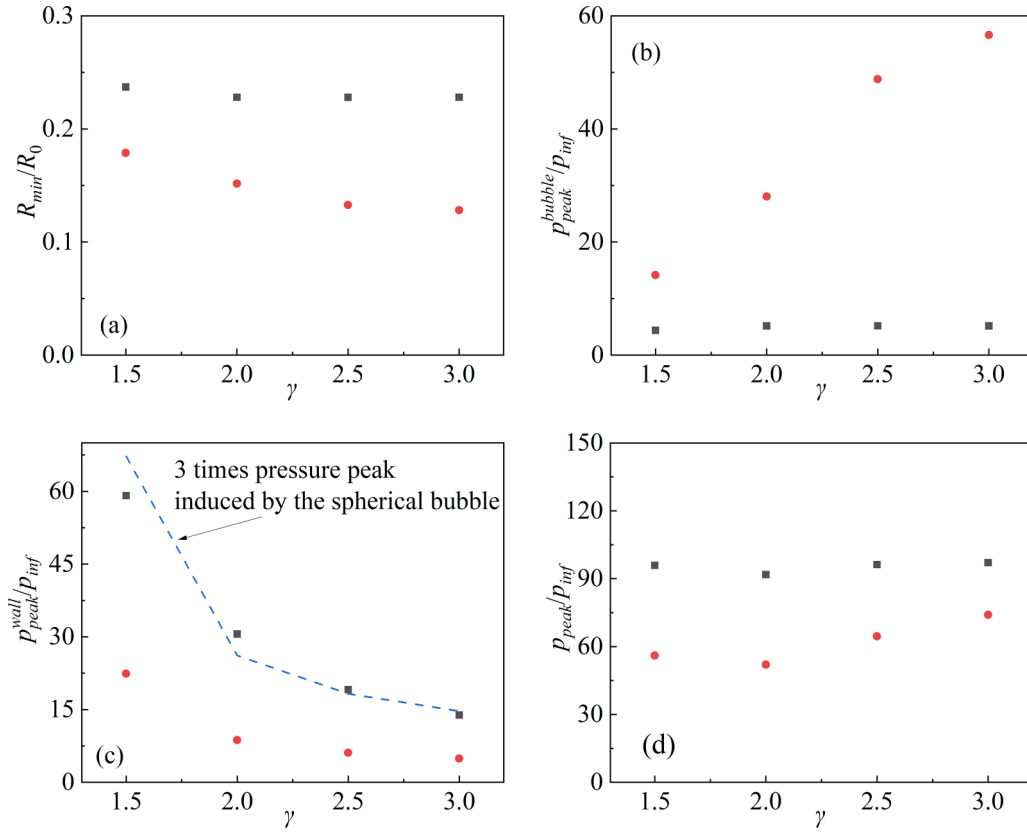


FIG. 15. Collapse of a toroidal bubble and a spherical bubble near a solid wall with different initial wall-bubble distances  $\gamma$ . (a) Minimum average bubble radius, (b) maximum average bubble pressure, (c) peak pressure induced on the solid wall, and (d) peak pressure induced in the computational domain. (■) Toroidal bubble; (●) spherical bubble.

than that induced by the spherical bubble. Finally, as depicted in Fig. 15(d), the maximum peak pressure in the flow field induced by the toroidal bubble consistently surpasses that induced by the spherical bubble across all wall-bubble distances examined.

Figure 16 presents the evolution of the  $y$  coordinate of the centroid of the toroidal bubble during its collapse near the

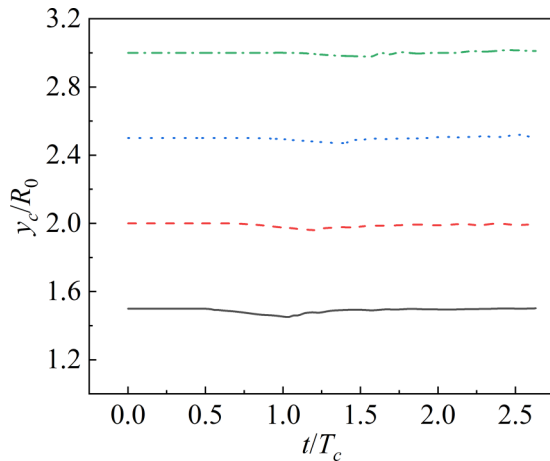


FIG. 16.  $Y$  coordinate of the centroid of a toroidal bubble ( $\varepsilon = 5$ ,  $p_{inf}/p_0 = 100$ ) with the initial wall-bubble distances (—)  $\gamma = 1.5$ ; (---)  $\gamma = 2.0$ ; (···)  $\gamma = 2.5$ ; (-.-.-)  $\gamma = 3.0$ .

solid wall. It can be found that for each case, the  $y$  coordinate values  $y_c$  remain almost unchanged; therefore we can conclude that the torus bubble does not move toward the solid wall during collapse when the initial wall-bubble distance  $\gamma = 1.5$ – $3.0$ .

#### IV. CONCLUSION

In this paper, we employ high-fidelity numerical simulation to examine the collapse of a toroidal bubble. To mitigate numerical dissipation near the discontinuities, we utilize the interface compression technique and the BVD reconstruction scheme. The accuracy of our approach is validated through theoretical analysis and experimental data. Our simulations provide valuable insights into the characteristics of shock waves and pressure loads during the collapse of a toroidal bubble. The main findings are outlined as follows.

(1) The collapse of a toroidal bubble shows significant differences compared to that of a spherical bubble. When a toroidal bubble collapses, the resulting shock wave consistently moves toward the axial line, resulting in significantly higher pressure (up to  $\sim 90p_{inf}$ ) along the central axis compared to a spherical bubble of equal volume. On the other hand, the pressure in the transverse direction is lower ( $\sim 3.5p_{inf}$ ) during the collapse of a toroidal bubble when compared to a spherical bubble.

(2) The aspect ratio  $\varepsilon$  has a significant impact on the peak pressure along the axial line, with larger  $\varepsilon$  resulting in higher

peak pressure, particularly at  $y = R_0$ . However, the effect of  $\varepsilon$  decreases for  $y \geq 2R_0$ , and has minimal effect on the peak pressure in the transverse direction.

(3) The numerical results indicate that the toroidal bubble collapses at a faster rate compared to the spherical bubble. Specifically, the Rayleigh collapse time for the toroidal bubble is approximately  $0.6T_c$ , whereas it is  $0.95T_c$  for the spherical bubble. However, as the bubble collapses to its minimum volume, the spherical bubble exhibits a smaller bubble radius and a higher bubble pressure than the toroidal bubble. Consequently, the collapse of a spherical bubble can be characterized as more violent in nature when compared to the collapse of a toroidal bubble.

(4) When a toroidal bubble collapses in the vicinity of a solid wall, the focused shock wave propagating along the torus center can result in high wall pressure. The presence of the solid wall has minimal influence on the deformation of the toroidal bubble. However, the wall pressure caused by the toroidal bubble is approximately three times greater than that caused by a spherical bubble with the same volume. Furthermore, the peak pressure in the flow field induced by

the toroidal bubble also exceeds that induced by the spherical bubble.

In conclusion, the numerical findings presented in this study provide valuable theoretical insights for the design of an underwater pressure vessel. These results have the potential to make a significant contribution to the development of enhanced strategies aimed at minimizing the detrimental effects of implosion events.

The data that support the findings of this study are available from the corresponding author upon reasonable request.

## ACKNOWLEDGMENTS

This work is supported by the National Natural Science Foundation of China (Grants No. 51979160 and No. 11902199), Hubei Provincial Natural Science Foundation of China (Grant No. 2024AFB400) and Top Young Talents of Ten Thousand Talents Plan, to which the authors are most grateful.

- 
- [1] Y. Cao and R. Macián-Juan, Numerical study of the central breakup behaviors of a large bubble rising in quiescent liquid, *Chem. Eng. Sci.* **225**, 115804 (2020).
- [2] D. M. Sharaf, A. R. Premkata, M. K. Tripathi, B. Karri, and K. C. Sahu, Shapes and paths of an air bubble rising in quiescent liquids, *Phys. Fluids* **29**, 122104 (2017).
- [3] E. Johnsen and T. Colonius, Numerical simulations of non-spherical bubble collapse, *J. Fluid Mech.* **629**, 231 (2009).
- [4] J. H. Niederhaus, J. Greenough, J. Oakley, D. Ranjan, M. H. Anderson, and R. Bonazza, A computational parameter study for the three-dimensional shock–bubble interaction, *J. Fluid Mech.* **594**, 85 (2008).
- [5] D. Ranjan, J. Oakley, and R. Bonazza, Shock-bubble interactions, *Annu. Rev. Fluid Mech.* **43**, 117 (2011).
- [6] J. R. Blake and D. Gibson, Growth and collapse of a vapour cavity near a free surface, *J. Fluid Mech.* **111**, 123 (1981).
- [7] A. M. Zhang, P. Cui, J. Cui, and Q. X. Wang, Experimental study on bubble dynamics subject to buoyancy, *J. Fluid Mech.* **776**, 137 (2015).
- [8] O. Supponen, P. Kobel, D. Obreschkow, and M. Farhat, The inner world of a collapsing bubble, *Phys. Fluids* **27**, 091113 (2015).
- [9] S. Zhang, S. P. Wang, and A. M. Zhang, Experimental study on the interaction between bubble and free surface using a high-voltage spark generator, *Phys. Fluids* **28**, 032109 (2016).
- [10] L. T. Liu, X. B. Chen, W. Q. Zhang, and A.-M. Zhang, Study on the transient characteristics of pulsation bubble near a free surface based on finite volume method and front tracking method, *Phys. Fluids* **32**, 052107 (2020).
- [11] M. Kornfeld and L. Suvorov, On the destructive action of cavitation, *J. Appl. Phys.* **15**, 495 (1944).
- [12] T. B. Benjamin and A. T. Ellis, A discussion on deformation of solids by the impact of liquids, and its relation to rain damage in aircraft and missiles, to blade erosion in steam turbines, and to cavitation erosion - The collapse of cavitation bubbles and the pressures thereby produced against solid boundaries, *Philos. Trans. R. Soc. London, Ser. A* **260**, 221 (1966).
- [13] M. S. Plesset and R. B. Chapman, Collapse of an initially spherical vapour cavity in the neighbourhood of a solid boundary, *J. Fluid Mech.* **47**, 283 (1971).
- [14] O. Lindau and W. Lauterborn, Cinematographic observation of the collapse and rebound of a laser-produced cavitation bubble near a wall, *J. Fluid Mech.* **479**, 327 (2003).
- [15] L. Liu, X. Yao, N. Liu, and F. L. Yu, Toroidal bubble dynamics near a solid wall at different Reynolds number, *Int. J. Multiphase Flow* **100**, 104 (2018).
- [16] G. Huang, M. Zhang, X. Ma, Q. Chang, C. Zheng, and B. Huang, Dynamic behavior of a single bubble between the free surface and rigid wall, *Ultrason. Sonochem.* **67**, 105147 (2020).
- [17] E. Ezzatneshan and H. Vaseghnia, Simulation of collapsing cavitation bubbles in various liquids by lattice Boltzmann model coupled with the Redlich-Kwong-Soave equation of state, *Phys. Rev. E* **102**, 053309 (2020).
- [18] X. Yang, C. Liu, D. Wan, and C. Hu, Numerical study of the shock wave and pressure induced by single bubble collapse near planar solid wall, *Phys. Fluids* **33**, 073311 (2021).
- [19] M. Rodriguez, S. A. Beig, C. N. Barbier, and E. Johnsen, Dynamics of an inertially collapsing gas bubble between two parallel, rigid walls, *J. Fluid Mech.* **946**, A43 (2022).
- [20] S. W. Fong, D. Adhikari, E. Klaseboer, and B. C. Khoo, Interactions of multiple spark-generated bubbles with phase differences, *Exp. Fluids* **46**, 705 (2009).
- [21] J. Luo and Z. Niu, Jet and shock wave from collapse of two cavitation bubbles, *Sci. Rep.* **9**, 1 (2019).
- [22] X. Yang, C. Liu, J. Li, M. Zhao, and C. Hu, Implosion of a bubble pair near a solid surface, *Phys. Rev. Fluids* **8**, 023602 (2023).
- [23] L. Zhang, J. Zhang, and J. Deng, Numerical investigation on the collapse of a bubble cluster near a solid wall, *Phys. Rev. E* **99**, 043108 (2019).

- [24] T. Trummer, S. H. Bryngelson, K. Schmidmayer, S. J. Schmidt, T. Colonius, and N. A. Adams, Near-surface dynamics of a gas bubble collapsing above a crevice, *J. Fluid Mech.* **899**, A16 (2020).
- [25] O. Supponen, D. Obreschkow, P. Kobel, M. Tinguely, N. Dorsaz, and M. Farhat, Shock waves from nonspherical cavitation bubbles, *Phys. Rev. Fluids* **2**, 093601 (2017).
- [26] J. Luo, W. Xu, and B. C. Khoo, Stratification effect of air bubble on the shock wave from the collapse of cavitation bubble, *J. Fluid Mech.* **919**, A16 (2021).
- [27] O. Supponen, D. Obreschkow, P. Kobel, and M. Farhat, Luminescence from cavitation bubbles deformed in uniform pressure gradients, *Phys. Rev. E* **96**, 033114 (2017).
- [28] N. Bempedelis and Y. Ventikos, Energy focusing in shock-collapsed bubble arrays, *J. Fluid Mech.* **900**, A44 (2020).
- [29] M. Alloul, B. Dollet, O. Stephan, E. Bossy, C. Quilliet, and P. Marmottant, Acoustic resonance frequencies of underwater toroidal bubbles, *Phys. Rev. Lett.* **129**, 134501 (2022).
- [30] K. S. Spratt, K. M. Lee, P. S. Wilson, and M. F. Hamilton, Acoustic scattering from a toroidal bubble, *JASA Express Lett.* **2**, 036001 (2022).
- [31] G. L. Chahine and P. F. Genoux, Collapse of a cavitating vortex ring, *J. Fluids Eng.* **105**, 400 (1983).
- [32] Y. Cao and R. Macián-Juan, Numerical investigation of central breakup of large bubble induced by liquid jet, *Phys. Fluids* **32**, 033302 (2020).
- [33] L. T. Liu, X. L. Yao, A. M. Zhang, and Y. Y. Chen, Numerical analysis of the jet stage of bubble near a solid wall using a front tracking method, *Phys. Fluids* **29**, 012105 (2017).
- [34] A. K. Kapila, R. Menikoff, J. B. Bdzil, S. F. Son, and D. S. Stewart, Two-phase modeling of deflagration-to-detonation transition in granular materials: Reduced equations, *Phys. Fluids* **13**, 3002 (2001).
- [35] Z. Sun, S. Inaba, and F. Xiao, Boundary variation diminishing (BVD) reconstruction: A new approach to improve Godunov schemes, *J. Comput. Phys.* **322**, 309 (2016).
- [36] X. Deng, S. Inaba, B. Xie, K.-M. Shyue, and F. Xiao, High fidelity discontinuity-resolving reconstruction for compressible multiphase flows with moving interfaces, *J. Comput. Phys.* **371**, 945 (2018).
- [37] G.-S. Jiang and C.-W. Shu, Efficient implementation of weighted ENO schemes, *J. Comput. Phys.* **126**, 202 (1996).
- [38] F. Xiao, Y. Honma, and T. Kono, A simple algebraic interface capturing scheme using hyperbolic tangent function, *Int. J. Numer. Methods Fluids* **48**, 1023 (2005).
- [39] A. Tiwari, J. B. Freund, and C. Pantano, A diffuse interface model with immiscibility preservation, *J. Comput. Phys.* **252**, 290 (2013).
- [40] R. Menikoff and B. J. Plohr, The Riemann problem for fluid flow of real materials, *Rev. Mod. Phys.* **61**, 75 (1989).
- [41] D. Rossinelli, B. Hejazialhosseini, P. Hadjidoukas, C. Bekas, A. Curioni, A. Bertsch, S. Futral, S. J. Schmidt, N. A. Adams, and P. Koumoutsakos, 11 PFLOP/s simulations of cloud cavitation collapse, in *Proceedings of the International Conference on High Performance Computing, Networking, Storage and Analysis* (Association for Computing Machinery, New York, 2013), pp. 1–13.
- [42] P. E. Hadjidoukas, D. Rossinelli, B. Hejazialhosseini, and P. Loumoutsakos, From 11 to 14.4 PFLOPs: Performance optimization for finite volume flow solver, in *Proceedings of the 3rd International Conference on Exascale Applications and Software* (Association for Computing Machinery, New York, 2015), pp. 7–12.
- [43] B. Van Leer, Towards the ultimate conservative difference scheme. V. A second-order sequel to Godunov's method, *J. Comput. Phys.* **32**, 101 (1979).
- [44] E. Johnsen and T. Colonius, Implementation of WENO schemes in compressible multicomponent flow problems, *J. Comput. Phys.* **219**, 715 (2006).
- [45] V. Coralic and T. Colonius, Finite-volume WENO scheme for viscous compressible multicomponent flows, *J. Comput. Phys.* **274**, 95 (2014).
- [46] D. I. Ketcheson, M. Parsani, and R. J. Leveque, High-order wave propagation algorithms for hyperbolic systems, *SIAM J. Sci. Comput.* **35**, A351 (2013).
- [47] E. F. Toro, *Riemann Solvers and Numerical Methods for Fluid Dynamics: A Practical Introduction* (Springer Science & Business Media, Berlin, 2009).
- [48] S. Gottlieb and C.-W. Shu, Total variation diminishing Runge-Kutta schemes, *Math. Comput.* **67**, 73 (1998).
- [49] X. Yang, C. Liu, J. Li, Y. Yang, M. Zhao, and C. Hu, Numerical study of liquid jet and shock wave induced by two-bubble collapse in open field, *Int. J. Multiphase Flow* **168**, 104584 (2023).
- [50] J. B. Keller and M. Miksis, Bubble oscillations of large amplitude, *J. Acoust. Soc. Am.* **68**, 628 (1980).
- [51] L. Rayleigh, VIII. On the pressure developed in a liquid during the collapse of a spherical cavity, *London, Edinburgh Dublin Philos. Mag. J. Sci.* **34**, 94 (1917).
- [52] K. Johansen, J. H. Song, K. Johnston, and P. Prentice, Deconvolution of acoustically detected bubble-collapse shock waves, *Ultrasonics* **73**, 144 (2017).